

X-Ray Observation on the Monoceros R2 Star-Forming Region with the Chandra ACIS-I Array

Hiroshi NAKAJIMA, Kensuke IMANISHI, Shin-ichiro TAKAGI, Katsuji KOYAMA

Department of Physics, Graduate School of Science, Kyoto University, Sakyo-ku, Kyoto 606-8502
nakajima@cr.scphys.kyoto-u.ac.jp, kensuke@cr.scphys.kyoto-u.ac.jp, takagi9@cr.scphys.kyoto-u.ac.jp,
koyama@cr.scphys.kyoto-u.ac.jp

and

Masahiro TSUJIMOTO

Department of Astronomy & Astrophysics, Pennsylvania State University,
525 Davey Lab., University Park, PA 16802, USA
tsujimot@astro.psu.edu

(Received 2002 November 29; accepted 2003 April 28)

Abstract

We report on the results of the Chandra ACIS-I observation on the central region of the Monoceros R2 cloud (Mon R2), a high-mass star-forming region (SFR) at a distance of 830 pc. With a deep exposure of ~ 100 ks, we detected 368 X-ray sources, $\sim 80\%$ of which were identified with the near-infrared (NIR) counterparts. We systematically analyzed the spectra and time variability of most of the X-ray emitting sources and provided a comprehensive X-ray source catalog for the first time. Using the J -, H -, and K -band magnitudes of the NIR counterparts, we estimated the evolutionary phase (classical T Tauri stars and weak-lined T Tauri stars) and the mass of the X-ray emitting sources, and analyzed the X-ray properties as a function of the age and mass. We found a marginal hint that classical T Tauri stars have a slightly higher temperature (2.4 keV) than that of weak-lined T Tauri stars (2.0 keV). A significant fraction of the high- and intermediate-mass sources have a time variability and high plasma temperatures (2.7 keV) similar to those of low-mass sources (2.0 keV). We performed the same analysis for other SFRs, the Orion Nebula Cluster and Orion Molecular Cloud-2/3, and obtained similar results to Mon R2. This supports the earlier results of this observation obtained by Kohno et al. (2002, ApJ, 567, 423) and Preibisch et al. (2002, A&A, 392, 945) that high- and intermediate-mass young stellar objects emit X-rays via magnetic activity. We also found a significant difference in the spatial distribution between X-ray and NIR sources.

Key words: ISM: stars — ISM: individual (Monoceros R2) — stars: formation — X-rays: stars

1. Introduction

Low-mass young stellar objects (YSOs) are classified along their evolutionary phases into classes 0, I, II, and III based on their infrared (IR) to sub-millimeter spectral energy distributions (Lada 1991; André et al. 1993; André, Montmerle 1994). Class 0 and I sources correspond to the youngest and evolved protostars, while class II and III sources roughly correspond to classical T Tauri stars (CTTSs) and weak-lined T Tauri stars (WTTSs), respectively. Low-mass TTSs (=CTTSs and WTTSs) were first discovered to emit significant X-rays with the Einstein observatory (Feigelson, DeCampli 1981; Feigelson, Kriss 1981; Montmerle et al. 1983). The following observations with ASCA and ROSAT found X-rays from class I sources (Koyama et al. 1994; Casanova et al. 1995; Koyama et al. 1996; Kamata et al. 1997; Grosso et al. 1997, 2000; Tsuboi 1999; Tsuboi et al. 2000; Grosso 2001). In addition, Tsuboi et al. (2001) reported on the hard X-ray emission from class 0 candidates using the Chandra X-ray Observatory (CXO). Thus, it is now widely known that low-mass YSOs commonly emit X-rays during most of their evolutionary phases. Although it is not clear for class 0 sources, X-ray emission from most YSOs is explained by a thermal plasma with temperatures of 1 to a few keV and rapid time variances, which are similar to those of the solar X-rays. Accordingly, the X-ray origin is generally thought to be solar-type magnetic activity: amplification of the magnetic field followed by magnetic reconnection associated with the stellar convection layer and differential rotation (Feigelson, DeCampli 1981; Montmerle et al. 1983). However, whether or not the X-ray emission differs systematically along the evolutionary phases and stellar masses is not yet known.

On the other hand, the X-ray emission of high-mass main-sequence (MS) stars is described by a thin thermal plasma model with relatively soft temperatures of less than 1 keV, and shows moderate variability. Lucy and White (1980) proposed that these features are due to the plasma heating attributable to the collision of the accelerated stellar wind with circumstellar matter. However, our understanding of X-ray emission from high- and intermediate-mass YSOs is largely behind the low-mass sources and high-mass MS stars, because the former evolve very quickly and the population is small; hence, they constitute fewer or more distant samples than those of low-mass YSOs. Since YSOs are generally located in dense cloud cores, not only optical/near-infrared (NIR) light but also soft X-rays suffer large extinction. Accordingly, hard X-ray imaging instruments are essential to resolve embedded YSOs in the cores. The CXO (Weisskopf et al. 2002), with a high spatial resolution, large field of view (FOV), wide energy range and moderate energy resolution, provides the best instruments for observing the star-forming regions (SFRs).

The Monoceros R2 cloud (hereafter Mon R2) is one of the closest high-mass SFRs, which is located at a distance of 830 pc (Racine 1968). The cloud age is ~ 1 Myr (Carpenter et al. 1997), providing numerous YSOs over a wide range of ages from protostars to WTTSs. The

core mass is $\sim 1000 M_{\odot}$ (Tafalla et al. 1997), which is two orders of magnitude larger than those of the cores of low- to intermediate-mass SFRs. Thus, Mon R2 is a good candidate for a systematic study of the X-ray emission along the evolutionary phases and a study of high-mass star formation.

The first X-ray observation on Mon R2 was made with the ROSAT satellite (Gregorio-Hetem et al. 1998). However, the spatial resolution was limited to resolve individual YSOs in the Mon R2 core. Also, a short exposure (~ 9500 s) observation and poor sensitivity in the hard energy band limited the possibility to detect most of the embedded YSOs. Then, the ASCA observation on Mon R2 (Hamaguchi et al. 2000) also could not resolve individual YSOs due to the limited spatial resolution of $\sim 1'$. Recently, Kohno et al. (2002) performed a CXO observation and resolved X-rays from many YSOs for the first time. The earlier results have already been reported by Kohno et al. (2002) and Preibisch et al. (2002), but concentrated only on the central $3'2 \times 3'2$ region. This paper reports on a follow-up analysis of the CXO data in the entire cloud core and the NIR cluster of Mon R2. The purposes of this paper are (1) to make a comprehensive X-ray catalog, (2) to discuss the X-ray properties as a function of the evolutionary phases and the masses of YSOs, and (3) to discuss the characteristics of X-ray sources by comparing the spatial distribution of the X-ray and NIR sources.

2. Observation

Mon R2 was observed with the Advanced CCD Imaging Spectrometer (ACIS) on board the CXO on 2000 December 2–4. The ACIS-I array, comprising four abutted front-illuminated X-ray CCDs, covered the entire cloud core and the NIR cluster of Mon R2. The telescope optical axis position on the ACIS-I array was R.A. = $06^{\text{h}}07^{\text{m}}50^{\text{s}}86$, Decl. = $-06^{\circ}22'50''0$ (J2000). A high spatial resolution of $\sim 0''.5$, a large field of view (FOV) of $17'.4 \times 17'.4$, a wide energy range of 0.2–10.0 keV with a moderate energy resolution ($\Delta E \sim 200$ eV at $E = 6$ keV), and a time resolution of 3.2 s provide us with high-quality and uniform samples of YSOs in the cloud. We used the level 2 data provided by the pipeline processing at the Chandra X-ray Center. Besides, we removed those events due to charged particles and hot and flickering pixels. The effective exposure time was then ~ 100 ks.

3. Analysis

3.1. Source Detection

Figure 1 shows an ACIS-I image of the entire cloud core and the NIR cluster of Mon R2 overlaid on a ^{13}CO ($J=1-0$) intensity map (Loren 1977). For source detection, we used the *wavdetect* program in the CIAO package version 2.2¹ in the 0.5–10.0 keV band with a threshold significance of 10^{-6} and wavelet scales from 1 to 16 pixels in multiples of $\sqrt{2}$. In

¹ See <http://asc.harvard.edu/ciao/>.

order to study the spectra and timing with reasonable statistics, we discarded the sources with X-ray counts of less than three-times the background. We then detected 368 sources in the ACIS-I FOV. The X-ray photons of each source were accumulated from a circular region with a radius of $0''.7$ – $15''.4$, depending on the point spread function (PSF), which is a function of the angular distance from the telescope optical axis. The background photons were extracted from a source-free circle of $\sim 42''$ in radius.

3.2. Correlation with the NIR Sources

To search for the NIR counterparts of the CXO sources, we used the Point Source Catalog in the 2MASS Second Incremental Data Release², and the results of SQUIID and IRCAM3 observations (Carpenter et al. 1997). SQUIID was mounted at the Cassegrain focus of the 1.3 m telescope in the Kit Peak National Observatory, which simultaneously takes *J*-, *H*-, and *K*-band images using 256×256 PtSi arrays (Ellis et al. 1993). The pixel scale is $1''.36$ providing a FOV of $5'.8 \times 5'.8$. The mosaic consists of 3×3 frames, and hence the SQUIID observation obtained a $\sim 15' \times 15'$ mosaic image with the photometric mode centered on Mon R2. IRCAM3 at UKIRT (United Kingdom Infra-Red Telescope) utilizes a 256×256 InSb array. The pixel scale is $0''.286$, providing a FOV of $1'.2 \times 1'.2$. The observation consisted of 3×3 grid mosaics; hence, the IRCAM3 observation presented *J*, *H*, *K*, and narrow-band *L* imaging photometry of the central $\sim 3'.2 \times 3'.2$ region of Mon R2 more deeply than the SQUIID observation. The 5σ completeness limits in the *K*-band images were 14.5 mag and 16.6 mag for the SQUIID and IRCAM3 observations, respectively (Carpenter et al. 1997). On the other hand, 2MASS has the K_s -band limit of 14.3 mag. Because the position accuracy of 2MASS (the r.m.s. uncertainty of $\sim 0''.1$) is better than those of SQUIID ($0''.3$) and IRCAM3 ($\sim 0''.13$), we used the 2MASS frame as the standard frame. The distribution of the positional differences between SQUIID, IRCAM3, and 2MASS could be approximated by a two-dimensional Gaussian in the Δ R.A.– Δ Decl. plane with the center at Δ R.A. $\sim 0''.65$ and Δ Decl. $\sim 0''.06$. We hence fine-tuned the SQUIID and IRCAM3 frames so that the center of the Gaussian would come to the zero position of the 2MASS frame.

We picked up the closest NIR source from each X-ray source and did vice versa. Using the thus-selected closest pairs of NIR and X-ray sources, we fine-tuned the ACIS-I frame by shifting $-0''.87$ in R.A. and $-0''.75$ in Decl. to match the 2MASS frame. We then searched for the closest pairs of NIR and X-ray sources again. Among these pairs, we identified counterpart pairs under the criterion that the angular distance between the X-ray and the NIR source is smaller than the root mean square of the position uncertainty derived by the wavdetect program and the radius of the PSF.

Finally, 245 X-ray sources were identified with the NIR counterparts in the SQUIID and IRCAM3 databases, and outside of the FOV of SQUIID, additional 45 X-ray sources were identi-

² See <http://www.ipac.caltech.edu/2mass/>.

fied with the 2MASS sources (see figure 2). Assuming a random distribution of the NIR sources, the chance coincidence that any of the NIR sources fall in an X-ray source region is estimated to be $\sim 0.6\%$; hence, the false identification is expected to be less than two sources. The fine-tuned source positions, background-subtracted photon counts in the 0.5–10.0 keV band, and the name of the NIR counterparts are given in table 1.

3.3. Spectral and Timing Analyses

For bright 126 sources having more than 50 photons after background subtraction (hereafter “bright sources”), we performed spectral and timing analyses using XSPEC version 10.0 in XANADU.³ The X-ray spectra were fitted by a thin-thermal plasma model with three free parameters: the absorption column density (N_{H}), plasma temperature (kT), and normalization. Since the statistics are limited for most sources, the chemical abundance was fixed to be 0.3 solar according to previous reports (Kohno et al. 2002; Feigelson et al. 2002; Getman et al. 2002). The best-fit parameters and relevant physical values are listed in table 2 with their 90% errors in parentheses. The distributions of N_{H} , kT , and L_{X} of bright sources are shown with their mean value and that weighed with the errors (Bevington, Robinson 1992) in figures 3, 4, and 5, respectively.

We then made light curves of the bright sources in the 0.5–10.0 keV band. To study the time variability, we applied the Kolmogorov–Smirnov test (Press et al. 1988); then, 49 out of 126 sources were found to be time variables with more than 99% confidence. The significance levels of the time variability are listed in table 2. Most of the variable sources exhibit a flare-like event with a fast rise and slow decay.

4. Discussion

4.1. Cloud Members

We examined whether or not the detected 368 X-ray sources are cloud members by checking their N_{H} values and K -band magnitudes. The absorption column density of the interstellar medium to Mon R2 is estimated to be $\sim 2.6 \times 10^{21} \text{ cm}^{-2}$, assuming the density of the interstellar medium to be 1 cm^{-3} . Since the N_{H} values of most X-ray sources exceed this value (figure 3), they should be located in or behind the cloud, although the limited photon counts can not give firm constraints. Most of the background galaxies have $K \gtrsim 17 \text{ mag}$ (Tsujiimoto et al. 2002), while the K -band limit of NIR sources is 16.6 mag. We thus suspect that most of the NIR identified X-ray sources are cloud members.

For all of the ACIS sources, we searched for possible binary systems by checking whether or not two or more NIR sources were located within a radius of three-times the PSF. We used 2MASS and IRCAM3 catalogs, which have comparable pixel scales of $1''.0$ and $0''.3$ compared

³ See (<http://heasarc.gsfc.nasa.gov/docs/software/lheasoft/>).

with that of ACIS of $0''.5$, and found that only one source, #151, has two NIR counterparts separated by $1''.1$ (or ~ 900 AU). This separation, however, is one order of magnitude larger than the typical separation of binaries (Giannuzzi 1989); hence, these two NIRs may not be a binary system.

4.2. Comparison with Previous X-ray Observations and Studies

In order to make a comprehensive discussion about X-ray emitting sources in Mon R2, we compared our results with those of previous studies.

In a ROSAT/PSPC observation, Gregorio-Hetem et al. (1998) found 23 X-ray point sources in the FOV of ACIS-I. We searched for ACIS counterparts within a radius of $5''.0$ from each PSPC source (position accuracy $\sim 10''$) and found seven counterparts. We also found five additional possible counterparts relaxing the criterion radius to the position error of each PSPC source (table 1). For the remaining 11 sources, we did not find significant X-rays. This may have been due to a long-time variability, possibly several years, as can be seen in the Sun.

There are some sources that are missing in table 1, but are listed in Kohno et al. (2002). This discrepancy arises from the difference in the source detection algorithm. In Kohno et al. (2002), after executing the wavdetect program, they detected 12 additional sources with a visual inspection above the 5σ confidence level. However, in this paper, we did not perform such an inspection, but excluded 34 sources under the criterion that they should have the source-significance level of more than three. Moreover, since we ran the wavdetect only for the total energy band image, some sources detected only in the soft band (0.5–2.0 keV) or hard band (2.0–10.0 keV) in Kohno et al. (2002) were missed in this study. We also compared our results of four intermediate- and high-mass YSOs (a_s , IRS1SW, IRS2, and IRS3NE) with those in Kohno et al. (2002). We do not report on X-rays from the position of a_s , although Kohno et al. (2002) found a counterpart within a $1''$ radius. We certainly found an X-ray source at a distance of $0''.54$ from a_s , which is larger than our criterion radius of identification at the position of a_s of $0''.5$ based on the error radius derived by the wavdetect program. We, hence, do not regard this X-ray source as a counterpart of a_s . For IRS1SW, IRS2, and IRS3NE, we obtained almost the same results as that of Kohno et al. (2002). Based on the positions in the color–color and color–magnitude diagrams (subsections 4.3 and 4.4), IRS1SW is classified as a high- or intermediate-mass CTTS, and IRS2 has a larger K -band excess than CTTSs. Because IRS3NE is saturated at the K band, the reliable K -band magnitude can not be obtained. However, based on the J - and H -band magnitudes, this is classified as a high- or intermediate-mass source.

Preibisch et al. (2002) resolved a multiple IRS3 source into three individual IR sources (IRS3A=IRS3S, IRS3C=IRS3NE, and IRS3E=CMDSH278) by their deep observation using HST/NICMOS, and found that all of the sources emit X-rays using the same dataset as ours. We found five photons at the NIR position of IRS3S. However, these photons may not be

from IRS3 because of severe contamination from the bright source #207 (=IRS3NE/IRS3C). IRS3E, which corresponds to #202, is classified as a low-mass CTTS, as also shown in figure 2 in Preibisch et al. (2002).

4.3. X-Ray Properties along the Evolutionary Phases

We classified the 247 X-ray sources that have J -, H -, and K -band counterparts (hereafter “NIR-bright sources”) into CTTS and WTTS by the following criterion. Using the NIR data, we made the $(J - H)/(H - K)$ color-color diagram shown in figure 6, where the colors were transformed into the CIT (California Institute of Technology) system (Bessel, Brett 1988) with a formula given by Carpenter (2001). The thin solid curves are the intrinsic colors of giant and dwarf stars (Tokunaga 2000), while the de-reddened locus (thick solid line) for CTTSs was taken from Meyer et al. (1997). We assumed the slope of the reddening line to be $E(J - H)/E(H - K) = 1.63$ (Martin, Whittet 1990), as given by the dashed lines. Since CTTSs are surrounded by cold accretion disks, they generally have larger K -values than WTTSs. Therefore, we regard the sources located between the middle and the right reddening lines and above the CTTS locus as CTTSs, while sources located between the left and middle reddening lines are regarded as WTTSs. We obtained 57 and 164 sources with this classification. The remaining 26 sources located in other regions could not be classified. The expected errors in the classification are presented by Meyer et al. (1997). They concluded that approximately 1/3 of the CTTSs would occupy the region of the WTTSs. However, in this paper, we use the terms “CTTSs” and “WTTSs” for plainness.

Excluding the unclassified sources, the number of bright sources and the averaged X-ray properties in each evolutionary phase are listed in table 3. We can see a higher kT for CTTSs (3.1 keV) than WTTSs (1.9 keV). However, there should be a selection bias in favor of a less-absorbed WTTS. Then, we also derived the averaged kT for the sources that had a N_{H} value less than 10^{22} cm^{-2} . Nevertheless, the kT of CTTSs (2.4 keV) is still slightly higher than that of WTTSs (2.0 keV). The confidence level of the difference between the two distributions of kT is estimated to be 87.6% using the ASURV statistical software package (ver.1.2).⁴ In order to examine this feature for other SFRs, we performed the same analysis using the published CXO catalogs of the Orion Nebula Cluster (hereafter ONC, Feigelson et al. 2002) and the Orion Molecular Cloud-2/3 (hereafter OMC-2/3, Tsujimoto et al. 2002), other sites of high- and intermediate-mass star formation. In identifying the 2MASS counterpart of X-ray sources in ONC, we defined the criterion that the angular separation of X-ray and NIR pairs is smaller than the solid line in figure 2, which is the envelope curve of the source identification criterion for Mon R2. For OMC-2/3, we used sources that were already identified with 2MASS sources by Tsujimoto et al. (2002). We then classified the sources with the same criterion as applied for Mon R2 and compared the mean X-ray temperature for each group, as shown in table 3.

⁴ See <http://www.astro.psu.edu/statcodes/>.

We again confirmed that the results similar to Mon R2; kT of CTTSs is slightly higher than that of WTTSs. The confidence levels of difference between the two distributions of kT are $> 99.9\%$ and 46.2% , respectively. Although the significance level is not high enough, except for ONC, we concluded that there is a marginal trend that kT of CTTSs is higher than that of WTTSs for all of the clouds (Mon R2, ONC, and OMC-2/3). This fact indicates that there is some changes between CTTSs and WTTSs in a physical process for the X-ray emission. In the case of YSO flares, Imanishi et al. (2003) reported that younger sources show a higher kT than evolved sources using a high-quality sample in the ρ Ophiuchi low-mass SFR. From a systematic study on the time profile of these flares, they concluded that the magnetic field gradually declines along the evolutionary phases, because the magnetic field strength has a positive correlation with kT (Shibata, Yokoyama 2002). For Mon R2, we can not discuss the flare and quiescent phases separately because of the limited photon counts. Future observations with a deep exposure time will reveal whether a similar effect can also be seen in Mon R2.

4.4. X-ray Properties of Different Stellar Masses

We divided the NIR-bright sources into two mass ranges, defined as $M > 2.0 M_{\odot}$ (high- and intermediate-mass), and $M < 2.0 M_{\odot}$ (low-mass) by the following criterion. In the $J/(J - H)$ color-magnitude diagram (figure 7), the 1 Myr isochrone curve of $0.02 M_{\odot}$ to $3.0 M_{\odot}$ sources (Baraffe et al. 1998; Siess et al. 2000) is shown by the solid line. We assumed the slope of the reddening line to be $A_J/E(J - H) = 2.26$ (Martin, Whittet 1990). We regard the sources located above the reddening line of stars with the mass of $2.0 M_{\odot}$ (dashed line) and rightward from the isochrone curve (solid curve) as high- and intermediate-mass sources, while sources below the reddening line and rightward from the isochrone curve to be low-mass sources. We then classified 10 and 230 sources into high- and intermediate-mass sources, and low-mass sources, respectively. The seven sources located leftward of the isochrone curve could not be classified. Excluding the seven unclassified sources, the number of bright sources and the averaged X-ray properties of each mass range are given in table 4. The N_{H} value for the low-mass sources are significantly smaller than that of the high- and intermediate-mass sources. This tendency may be due to the bias effect; the low-mass sources with large absorption come more easily below the detection limit compared to those of the high- and intermediate-mass sources, because the former has a systematically lower L_{X} than the latter (Kohno et al. 2002).

Since we found a high kT (2.7 keV) of the high- and intermediate-mass sources similar to that of the low-mass sources (2.0 keV), we also performed the same analysis for ONC and OMC-2/3, and found similar results to Mon R2 (table 4). Moreover, a significant fraction of the high- and intermediate-mass sources show a rapid time variability. These results indicate that the X-ray emitting process of high- and intermediate-mass YSOs is the same as that of the low-mass sources, i.e., magnetic activity (Kohno et al. 2002; Preibisch et al. 2002). Because high- and intermediate-mass YSOs lack surface convection layers (Palla, Stahler 1993), the convective

dynamo process may not work. What kind of the magnetic amplification mechanism is working in high- and intermediate-mass YSOs is still an open question.

4.5. *The Spatial Distribution of X-Ray Sources*

The spatial distribution of X-ray sources in Mon R2 seems to be elongated in the same direction as the ^{13}CO intensity structure, from north to south (figure 1). We examined whether or not the X-ray and NIR source distributions have the same structures as that of ^{13}CO by evaluating the correlation coefficient R (Bevington, Robinson 1992). We defined two source groups: those detected by X-rays and NIR. We set the x - and y -axis along the edge of the ACIS-I FOV, and calculated R for each source group separately. We then obtained $R = -0.19$ and -0.04 for the X-ray detected group and the NIR-detected group, respectively. In order to estimate the significance level, we randomly distributed the same number of test sources as those of X-ray and NIR in the x - y plane by 10000 times, and evaluated R . We then estimated the significance levels to be 3.7σ and 1.3σ , for the X-ray and NIR sources, respectively. We also derived R for sources that are detected by NIR, but not by X-ray, and obtained $R = -0.03$, the significance level of which is 1.0σ . Considering the significance levels, the distribution of the X-ray sources has a more elongated structure than that of NIR. This supports the observational review of Feigelson and Montmerle (1999) asserting that X-rays are a homogeneous tracer of all stages of YSOs, while the X-ray emission decreases as sources are approaching to the main-sequence stage. We confirmed this fact quantitatively for the first time by comparing the spatial distribution of X-ray sources and NIR sources.

5. Summary

We summarize the analysis of the 100 ks observation on Mon R2 with CXO ACIS-I as follows:

1. We detected 368 X-ray sources from the cloud and performed spectral and timing analyses for most of the sources. This provided one of the largest catalogs of X-ray sources in an SFR.
2. About 80% of the detected X-ray sources have NIR counterparts in the catalogs of 2MASS, SQUID, and IRCAM3. From their N_{H} and K -band magnitudes, we conclude that most of these NIR-identified X-ray sources are likely cloud members.
3. We classified the cloud members into CTTSs and WTTSs using a $(J - H)/(H - K)$ color-color diagram and compared the fractions of the X-ray time variability, averaged absorption, and temperature. We found a marginal trend that the temperatures of CTTSs are slightly higher than those of WTTSs. We performed the same analysis for the ONC and OMC-2/3 members, and obtained similar results as Mon R2. Thus, the physical structure of X-ray emission may change from CTTS to WTTS.
4. We divided the cloud members into high-, intermediate-, and low-mass sources based on

a $J/(J - H)$ color–magnitude diagram, and compared the averaged X-ray properties. A significant fraction of the high- and intermediate-mass sources are time variable and exhibit a high-temperature plasma as those of low-mass sources. This supports the earlier results by Kohno et al. (2002) and Preibisch et al. (2002) that high- and intermediate-mass YSOs emit X-rays via magnetic activity.

5. We performed an imaging analysis of the entire cloud core and the NIR cluster of Mon R2. We then found a significant difference in the spatial distribution between X-ray and NIR sources. We confirmed that X-rays can be used as a homogeneous tracer of all the stages of YSOs, as asserted by Feigelson and Montmerle (1999), and that the X-ray emission decreases as sources are approaching the main-sequence stage.

References

- André, P., Ward-Thompson, D., & Barsony, M. 1993, *ApJ*, 406, 122
- André, P., & Montmerle, T. 1994, *ApJ*, 420, 837
- Baraffe, I., Chabrier, G., Allard, F., & Hauschildt, P. H. 1998, *A&A*, 337, 403
- Beckwith, S., Evans, N. J., II, Becklin, E. E., & Neugebauer, G. 1976, *ApJ*, 208, 390
- Bessell, M. S., & Brett, J. M. 1988, *PASP*, 100, 1134
- Bevington, P. R. & Robinson, D. K. 1992, *Data Reduction and Error Analysis for the Physical Sciences*, 2d ed. (Boston: WCB/McGraw-Hill), p.53,198
- Carpenter, J. M. 2001, *AJ*, 121, 2851
- Carpenter, J. M., Meyer, M. R., Dougados, C., Strom, S. E., & Hillenbrand, L. A. 1997, *AJ*, 114, 198
- Casanova, S., Montmerle, T., Feigelson, E. D., & André, P. 1995, *ApJ*, 439, 752
- Ellis, T., et al. 1993, *Proc. SPIE*, 1765, 94
- Feigelson, E. D., Broos, P., Gaffney, J. A., III, Garmire, G., Hillenbrand, L. A., Pravdo, S. H., Townsley, L., & Tsuboi, Y. 2002, *ApJ*, 574, 258
- Feigelson, E. D., & DeCampli, W. M. 1981, *ApJ*, 243, L89
- Feigelson, E. D., & Kriss, G. A. 1981, *ApJ*, 248, L35
- Feigelson, E. D., & Montmerle, T. 1999, *ARA&A*, 37, 363
- Getman, K. V., Feigelson, E. D., Townsley, L., Bally, J., Lada, C. J., & Reipurth, B. 2002, *ApJ*, 575, 354
- Giannuzzi, M. A. 1989, *Ap&SS*, 161, 241
- Gregorio-Hetem, J., Montmerle, T., Casanova, S., & Feigelson, E. D. 1998, *A&A*, 331, 193
- Grosso, N. 2001, *A&A*, 370, L22
- Grosso, N., Montmerle, T., Feigelson, E. D., André, P., Casanova, S., & Gregorio-Hetem, J. 1997, *Nature*, 387, 56
- Grosso, N., Montmerle, T., Bontemps, S., André, P., & Feigelson, E. D. 2000, *A&A*, 359, 113
- Hamaguchi, K., Tsuboi, Y., & Koyama, K. 2000, *Adv. Space Res.*, 25, 531
- Howard, E. M., Pipher, J. L., & Forrest, W. J. 1994, *ApJ*, 425, 707
- Imanishi, K., Nakajima H., Tsujimoto, M., Koyama, K., & Tsuboi, Y. 2003, *PASJ*, 55, No.3

- Kamata, Y., Koyama, K., Tsuboi, Y., & Yamauchi, S. 1997, PASJ, 49, 461
- Kohno, M., Koyama, K., & Hamaguchi, K. 2002, ApJ, 567, 423
- Koyama, K., Hamaguchi, K., Ueno, S., Kobayashi, N., & Feigelson, E. D. 1996, PASJ, 48, L87
- Koyama, K., Maeda, Y., Ozaki, M., Ueno, S., Kamata, Y., Tawara, Y., Skinner, S., & Yamauchi, S. 1994, PASJ, 46, L125
- Lada, C. J., 1991, in *The Physics of Star Formation and Early Stellar Evolution*, NATO ASI, ed. C. J. Lada & N. D. Kylafis. (Dordrecht:Kluwer), 329
- Loren, R. B. 1977, ApJ, 215, 129
- Lucy, L. B., & White, R. L. 1980, ApJ, 241, 300
- Martin, P. G., & Whittet, D. C. B. 1990, ApJ, 357, 113
- Meyer, M. R., Calvet, N., & Hillenbrand, L. A. 1997, AJ, 114, 288
- Montmerle, T., Koch-Miramond, L., Falgarone, E., & Grindlay, J. E. 1983, ApJ, 269, 182
- Palla, F., & Stahler, S. W. 1993, ApJ, 418, 414
- Preibisch, T., Balega, Y. Y., Schertl, D., & Weigelt, G. 2002, A&A, 392, 945
- Press, W. H., Flannery, B. P., Teukolsky, S. A., & Vetterling, W. T. 1988, *Numerical Recipes in C*, 1st ed. (New York: Cambridge Univ. Press), p.487
- Racine, R. 1968, AJ, 73, 233
- Shibata, K., & Yokoyama, T. 2002, ApJ, 577, 422
- Siess, L., Dufour, E., & Forestini, M. 2000, A&A, 358, 593
- Tafalla, M., Bachiller, R., Wright, M. C. H., & Welch, W. J. 1997, ApJ, 474, 329
- Tokunaga, A. T. 2000, in *Allen's Astrophysical Quantities*, 4th ed. ed. A. N. Cox (New York: Springer), p.143
- Tsuboi, Y. 1999, Ph.D. Thesis, Kyoto University
- Tsuboi, Y., Imanishi, K., Koyama, K., Grosso, N., & Montmerle, T. 2000, ApJ, 532, 1089
- Tsuboi, Y., Koyama, K., Hamaguchi, K., Tatematsu, K., Sekimoto, Y., Bally, J., & Reipurth, B. 2001, ApJ, 554, 734
- Tsujimoto, M., Koyama, K., Tsuboi, Y., Goto, M., & Kobayashi, N. 2002, ApJ, 566, 974
- Weisskopf, M. C., Brinkman, B., Canizares, C., Garmire, G., Murray, S., & Van Speybroeck, L. P. 2002, PASP, 114, 1

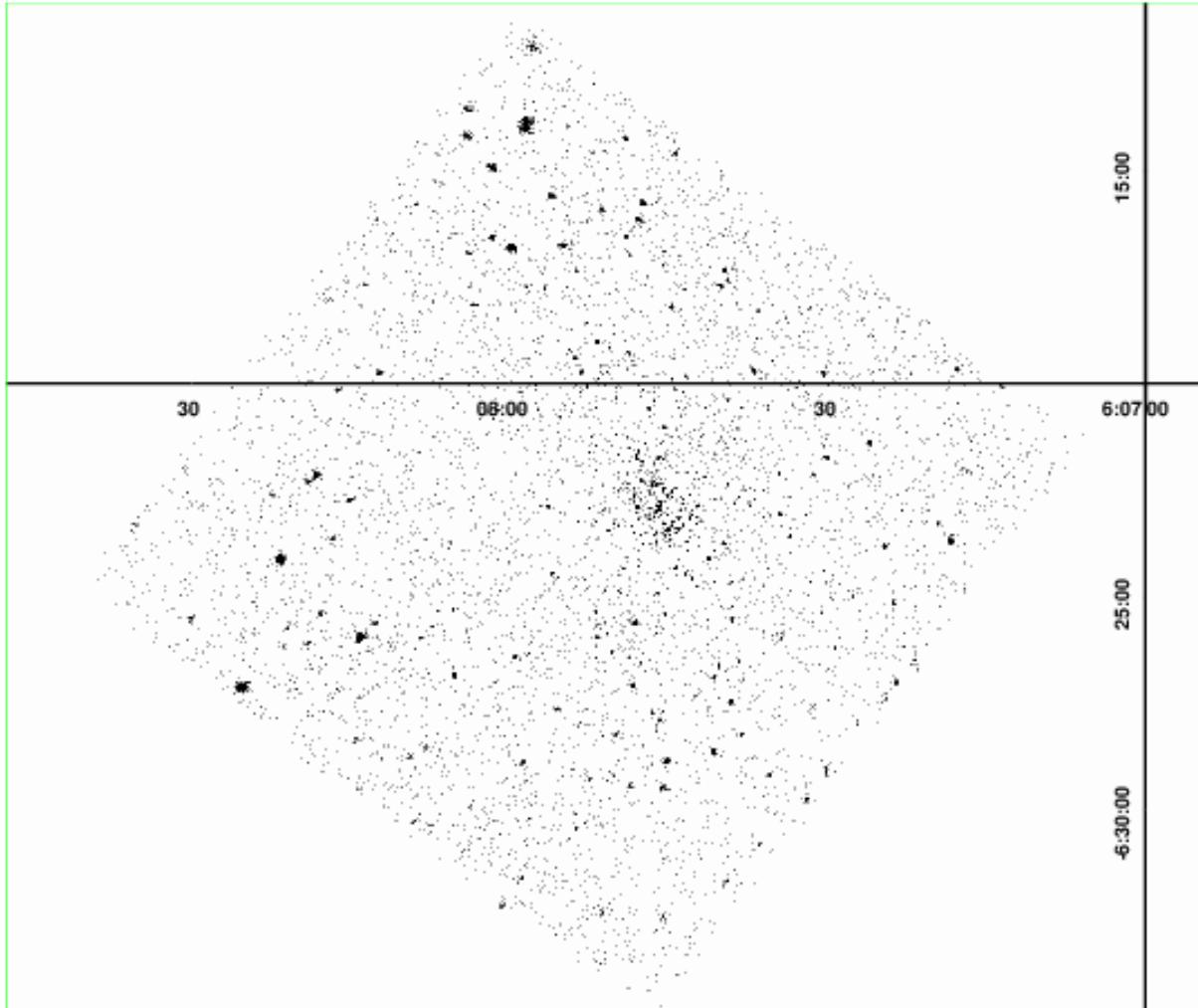


Fig. 1. ACIS-I image of the entire cloud core and the NIR cluster of Mon R2 (gray scale) overlaid on the ^{13}CO ($J=1-0$) intensity contour map with a beam size of $2'.6$ in diameter (Loren 1977). The square shows the ACIS-I FOV of $17'.4 \times 17'.4$. The background photons are extracted from the circular region. Contours are the antenna temperature at the intervals of 1 K. The plus indicates the position of the maximum temperature.

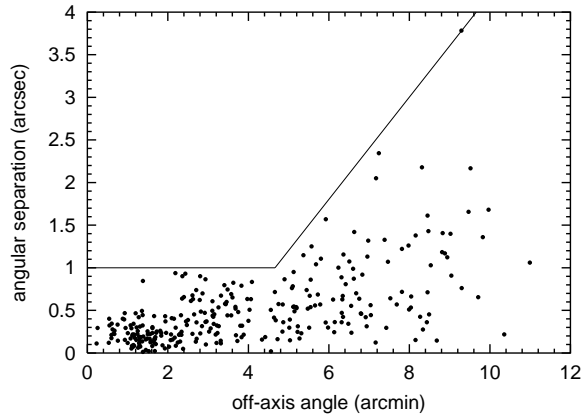


Fig. 2. Angular separation between X-ray sources and the NIR counterparts plotted as a function of the off-axis angle. The identification criterion for the ONC sources is shown by the solid line.

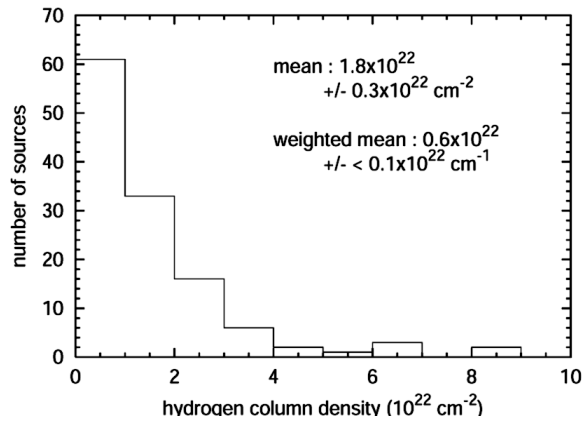


Fig. 3. Histogram of N_H of the bright sources. The mean value and that weighted with errors of the sources are shown.

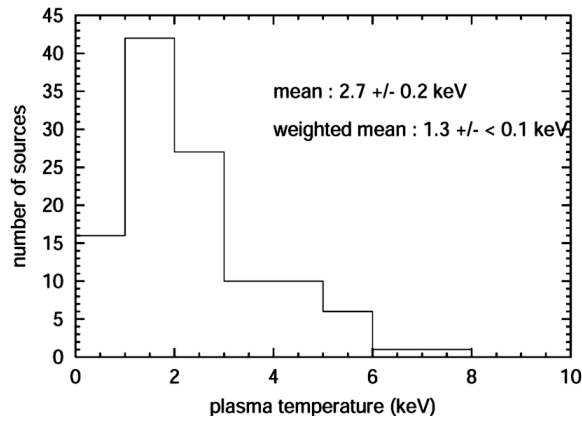


Fig. 4. Same as figure 3, but for kT .

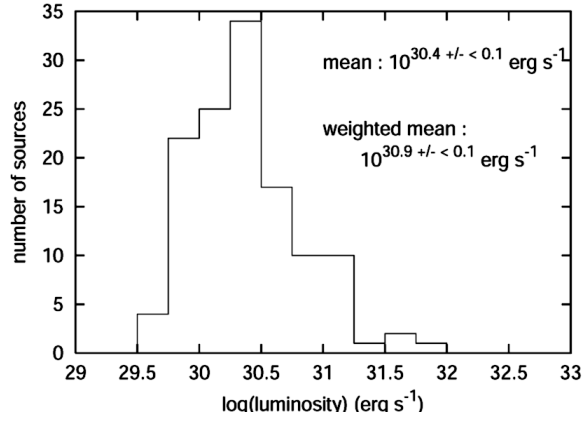


Fig. 5. Same as figure 3, but for L_X .

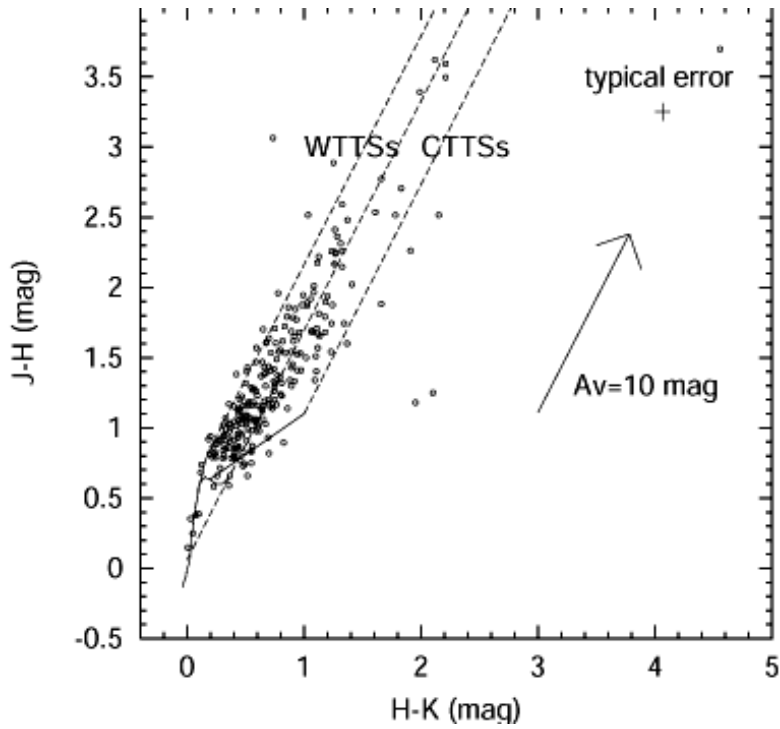


Fig. 6. $(J - H)/(H - K)$ color-color diagram in the CIT color system. X-ray sources that have J -, H -, and K -band counterparts are plotted with circles. The thick solid line indicates the de-reddened CTTS locus (Meyer et al. 1997). The intrinsic colors of giants and dwarfs are given by the thin solid curves (Tokunaga 2000). Reddening lines are given in dash (Martin, Whittet 1990).

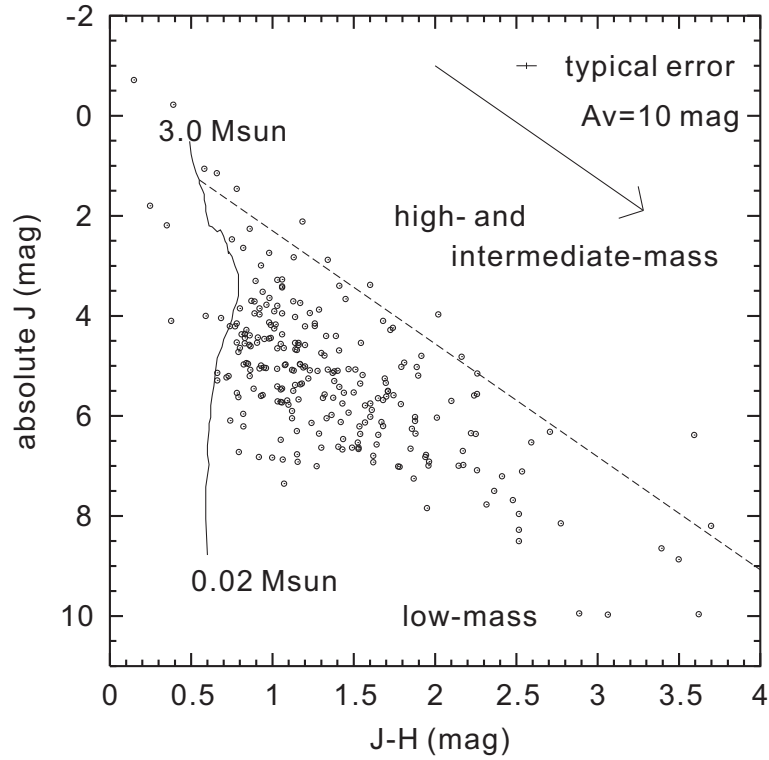


Fig. 7. Same as figure 6, but $J/(J - H)$ color–magnitude diagram. The term “absolute J ” indicates the J -band magnitude of each source is not corrected against the A_V value. The solid curve is the 1 Myr isochrone with $0.02 M_{\odot} < M < 3.0 M_{\odot}$ (Baraffe et al. 1998; Siess et al. 2000). The reddening line (dashed) is for stars with the mass of $2.0 M_{\odot}$ (Martin, Whittet 1990).

Table 1. Chandra X-ray sources and stellar counterparts.

ID	R.A.(J2000)* (mm ss)	Decl.(J2000)* (mm ss)	Count [†]	Identifications	
				X-ray [‡]	NIR [§]
1	07 13.48	20 06.7	13.6	...	2MASSI J0607134-062007
2	07 16.57	21 19.3	25.2
3	07 16.93	22 04.7	56.5	...	2MASSI J0607168-062205
4	07 17.69	19 43.4	54.8	...	2MASSI J0607177-061942
5	07 18.29	23 44.3	313.3	GMCF8	2MASSI J0607182-062344
6	07 19.47	23 20.4	55.7	...	CMDSH1005
7	07 20.58	23 16.0	22.6
8	07 21.73	26 32.1	61.5	...	CMDSH1031
9	07 22.88	23 01.5	17.8	...	CMDSH1039
10	07 23.46	27 03.0	90.3	...	CMDSH1041
11	07 23.66	25 11.5	61.8	...	CMDSH1043
12	07 24.38	27 22.1	32.5
13	07 24.54	23 51.7	80.0	...	CMDSH1047
14	07 25.97	21 25.4	124.8	...	CMDSH1057
15	07 27.03	27 56.7	10.5
16	07 28.01	18 03.1	17.2
17	07 29.23	26 13.9	52.8	...	CMDSH1075
18	07 29.90	21 46.8	85.5	...	CMDSH1082
19	07 30.06	29 08.3	60.3
20	07 30.07	24 43.6	13.1	...	CMDSH1086

* Right ascension and declination for all sources have the prefix of 06^h and −06° . Coordinates are corrected to the 2MASS frame.

† Background-subtracted X-ray photon counts in the 0.5–10.0 keV band.

‡ X-ray counterparts; (KKH): Kohno et al. (2002) and (GMCF): Gregorio-Hetem et al. (1998).

§ NIR counterparts; (CMDSH): Carpenter et al. (1997) and (2MASSI): 2MASS Point Source Catalog in the Second Incremental Data Release. NIR source names such as d_N and IRS4 are from Beckwith et al. (1976), Howard et al. (1994), and Carpenter et al. (1997).

Table 2. Results of timing and spectral analyses for bright sources.

ID	Variable probability*	N_{H}^{\dagger} (10^{22} cm^{-2})	kT^{\ddagger} (keV)	$\log(EM^{\S})^{\dagger}$ (cm^{-3})	$\log(L_{\text{X}}^{\parallel})^{\dagger}$ (erg s^{-1})
3	0.78	0.5 (0.1–0.9)	0.7 (0.5–1.1)	52.9 (52.8–53.0)	29.9 (29.8–30.0)
4	0.99	1.0 (...–...)	0.9 (...–...)	53.1 (53.0–53.2)	30.1 (30.0–30.2)
5	0.91	0.4 (0.3–0.6)	1.1 (1.0–1.3)	53.6 (53.6–53.7)	30.6 (30.5–30.6)
6	0.73	1.0 (...–...)	1.2 (...–...)	53.1 (53.0–53.2)	30.1 (30.0–30.2)
8	0.99	1.0 (0.2–1.4)	0.6 (0.4–1.7)	53.4 (53.2–53.4)	30.3 (30.2–30.4)
10	0.99	1.5 (0.6–2.0)	1.1 (0.7–2.4)	53.5 (53.4–53.6)	30.5 (30.4–30.5)
11	0.39	0.2 (0.0–0.5)	4.0 (...–37.8)	52.7 (52.6–52.8)	29.8 (29.7–29.9)
13	0.98	1.9 (1.0–3.5)	1.7 (0.9–2.6)	53.4 (53.3–53.5)	30.4 (30.3–30.5)
14	0.99	0.7 (0.3–1.3)	4.7 (1.8–...)	53.2 (53.1–53.3)	30.4 (30.3–30.4)
17	0.99	1.3 (...–...)	26.9 (...–...)	52.9 (52.8–53.0)	30.2 (30.0–30.3)
18	0.96	0.4 (0.2–0.8)	2.7 (1.4–8.1)	53.0 (52.9–53.1)	30.0 (29.9–30.1)
19	0.90	3.2 (1.8–6.1)	7.9 (...–...)	53.1 (53.0–53.2)	30.4 (30.2–30.5)
21	0.70	0.2 (0.1–0.5)	3.0 (1.5–19.0)	52.8 (52.7–52.9)	29.9 (29.8–30.0)
22	0.95	0.4 (...–...)	2.3 (...–...)	53.4 (53.4–53.5)	30.4 (30.4–30.5)
25	0.70	0.9 (...–...)	1.8 (1.0–5.1)	53.0 (52.9–53.1)	30.0 (29.9–30.1)
30	0.60	1.9 (1.3–3.0)	1.9 (1.2–3.7)	53.4 (53.3–53.5)	30.3 (30.2–30.4)
32	0.89	2.9 (2.2–...)	1.7 (1.2–2.6)	53.9 (53.8–54.0)	30.8 (30.8–30.9)
34	0.99	1.4 (0.7–2.6)	5.1 (1.9–...)	53.0 (52.9–53.1)	30.2 (30.0–30.2)
37	0.92	0.6 (0.3–1.6)	1.4 (1.0–2.1)	53.0 (52.9–53.1)	29.9 (29.8–30.0)
39	0.98	0.8 (0.4–1.5)	1.4 (1.1–2.4)	53.1 (53.0–53.2)	30.1 (30.0–30.2)
42	1.00	0.5 (0.4–...)	4.6 (2.8–6.7)	53.3 (53.3–53.4)	30.5 (30.4–30.5)
44	0.99	2.7 (1.6–4.9)	5.6 (1.6–...)	53.1 (53.0–53.2)	30.3 (30.2–30.4)
54	0.99	3.7 (2.6–5.3)	1.4 (1.0–2.3)	53.8 (53.7–53.9)	30.7 (30.6–30.8)
56	0.99	0.7 (0.6–0.8)	2.2 (1.8–2.7)	54.1 (54.1–54.2)	31.1 (31.1–31.2)
58	0.71	2.5 (1.7–3.6)	3.2 (1.7–...)	53.6 (53.5–53.6)	30.7 (30.6–30.7)
61	0.77	3.6 (2.1–5.9)	10.0	53.2 (53.1–53.3)	30.3 (30.2–30.4)
63	0.91	0.7 (0.3–1.5)	5.1 (2.0–55.7)	52.8 (52.7–52.9)	30.0 (29.9–30.1)
64	0.52	0.4 (0.1–0.7)	1.3 (1.0–2.0)	52.8 (52.6–52.9)	29.7 (29.6–29.8)
65	0.98	0.5 (0.2–0.9)	2.7 (1.3–10.3)	52.8 (52.7–52.9)	29.8 (29.7–29.9)
66	0.81	4.9 (2.8–15.7)	13.7 (...–...)	53.2 (53.1–53.3)	30.5 (30.3–30.5)
67	0.99	0.9 (0.1–1.4)	0.7 (0.3–2.3)	53.2 (53.1–53.3)	30.2 (30.1–30.3)
70	0.99	0.7 (0.2–1.0)	1.1 (0.9–1.8)	53.1 (53.0–53.1)	30.0 (29.9–30.1)
71	0.75	0.6 (0.2–1.1)	3.3 (1.6–25.7)	52.9 (52.8–52.9)	29.9 (29.8–30.0)
74	0.88	1.2 (0.9–1.4)	0.6 (0.4–0.8)	53.6 (53.5–53.7)	30.6 (30.5–30.7)
78	0.99	2.7 (1.6–4.3)	2.0 (1.1–4.2)	53.4 (53.3–53.5)	30.4 (30.3–30.5)
83	0.99	3.2 (2.0–4.8)	1.7 (1.0–3.1)	53.6 (53.5–53.7)	30.6 (30.5–30.7)
105	0.89	0.2 (0.1–0.4)	1.3 (1.0–1.6)	53.3 (53.3–53.4)	30.3 (30.2–30.3)
107	0.97	1.2 (0.6–2.0)	2.4 (1.1–7.5)	53.0 (52.9–53.1)	30.0 (29.9–30.1)
122	0.99	6.8 (5.3–9.1)	3.2 (1.9–5.3)	54.1 (54.1–54.2)	31.2 (31.2–31.3)
125	0.99	0.8 (0.3–1.1)	0.9 (0.6–1.2)	53.4 (53.3–53.4)	30.3 (30.2–30.4)
126	0.96	2.3 (1.5–3.6)	2.1 (1.1–4.4)	53.4 (53.3–53.5)	30.4 (30.3–30.5)
129	0.52	0.6 (0.4–...)	1.8 (1.3–2.0)	53.5 (53.5–53.6)	30.5 (30.4–30.5)
131	0.99	0.7 (0.4–1.0)	0.6 (...–...)	53.2 (53.0–53.2)	30.1 (30.0–30.2)
135	0.98	1.1 (0.3–1.9)	1.0 (0.4–3.0)	53.1 (53.0–53.2)	30.1 (30.0–30.2)
141	0.87	2.0 (1.8–2.4)	1.4 (...–...)	54.2 (54.2–54.3)	31.2 (31.1–31.2)
147	0.43	2.8 (1.0–4.5)	1.1 (0.7–1.7)	53.6 (53.5–53.7)	30.6 (30.5–30.7)
149	0.89	0.8 (0.3–1.5)	10.0	52.9 (52.7–53.1)	30.0 (29.8–30.1)
150	0.95	0.2 (0.1–0.4)	2.1 (1.3–4.1)	53.0 (53.0–53.1)	30.0 (30.0–30.1)
153	0.96	6.1 (2.5–13.3)	2.9 (...–...)	53.5 (53.4–53.6)	30.6 (30.5–30.7)

Table 2. (Continued)

ID	Variable probability*	N_{H}^{\dagger} (10^{22} cm^{-2})	kT^{\ddagger} (keV)	$\log(EM^{\S})^{\dagger}$ (cm^{-3})	$\log(L_{\text{X}}^{\parallel})^{\dagger}$ (erg s^{-1})
154	0.53	0.2 (0.1–0.7)	1.1 (0.6–1.6)	52.7 (52.6–52.8)	29.6 (29.5–29.7)
155	0.99	8.9 (5.0–11.3)	6.9 (...–...)	53.6 (53.5–53.6)	30.8 (30.7–30.9)
156	0.98	1.7 (1.5–2.0)	1.5 (...–...)	54.2 (54.2–54.2)	31.2 (31.1–31.2)
157	1.00	2.7 (2.1–3.4)	5.1 (3.3–13.6)	53.9 (53.8–53.9)	31.0 (31.0–31.1)
160	0.97	25.5 (10.3–41.9)	1.8 (0.9–5.8)	54.6 (54.5–54.6)	31.5 (31.4–31.6)
161	0.77	0.2 (0.0–1.0)	1.3 (0.5–1.9)	52.6 (52.5–52.7)	29.6 (29.5–29.7)
162	0.60	2.6 (1.4–3.3)	2.9 (1.8–10.4)	53.3 (53.2–53.4)	30.4 (30.3–30.5)
165	0.99	8.9 (5.6–15.6)	2.0 (0.9–3.6)	54.2 (54.1–54.2)	31.2 (31.1–31.2)
168	1.00	2.4 (1.4–3.8)	5.3 (2.2–26.0)	53.3 (53.2–53.4)	30.5 (30.4–30.5)
169	0.98	3.9 (2.5–6.0)	2.5 (1.2–...)	53.7 (53.6–53.8)	30.7 (30.7–30.8)
172	0.48	0.8 (0.2–1.4)	1.4 (0.9–3.3)	52.9 (52.8–53.0)	29.9 (29.7–30.0)
179	0.99	6.5 (3.6–11.3)	2.6 (1.2–8.3)	53.7 (53.6–53.8)	30.8 (30.7–30.8)
183	0.88	1.5 (0.9–2.6)	2.6 (1.5–6.9)	53.1 (53.0–53.2)	30.1 (30.0–30.2)
184	0.94	0.7 (0.2–1.7)	2.0 (1.0–5.7)	52.8 (52.7–52.9)	29.8 (29.7–29.9)
190	0.99	0.6 (0.3–1.4)	13.0 (...–...)	52.7 (52.6–52.8)	30.0 (29.9–30.1)
192	0.99	0.4 (0.2–0.8)	3.0 (1.7–...)	53.2 (53.2–53.3)	30.3 (30.2–30.4)
193	0.60	4.8 (3.0–7.0)	2.1 (1.1–4.3)	53.9 (53.8–53.9)	30.9 (30.8–30.9)
197	1.00	10.5 (5.6–20.1)	2.0 (...–8.3)	54.0 (53.9–54.1)	31.0 (30.9–31.1)
198	1.00	1.7 (1.2–2.5)	5.1 (2.8–...)	53.6 (53.5–53.6)	30.7 (30.7–30.8)
202	0.99	0.8 (0.2–2.4)	3.9 (...–...)	52.8 (52.7–52.9)	30.0 (29.8–30.0)
209	1.00	2.7 (2.5–2.9)	4.3 (3.6–5.2)	54.7 (54.7–54.7)	31.8 (31.8–31.9)
210	0.99	1.0 (...–2.2)	3.4 (...–62.0)	53.3 (53.2–53.4)	30.4 (30.3–30.5)
212	0.97	5.0 (3.2–...)	2.8 (...–...)	53.9 (53.9–54.0)	31.0 (30.9–31.0)
213	0.33	1.0 (0.7–1.3)	2.0 (...–...)	53.5 (53.5–53.6)	30.5 (30.5–30.6)
217	0.99	0.3 (0.2–0.4)	1.3 (1.1–1.5)	53.4 (53.3–53.4)	30.3 (30.3–30.4)
220	0.98	0.3 (0.1–0.6)	1.9 (1.3–2.8)	53.0 (52.9–53.0)	29.9 (29.8–30.0)
224	1.00	2.4 (1.4–3.6)	2.9 (1.6–...)	53.6 (53.5–53.7)	30.7 (30.6–30.7)
225	0.93	1.8 (1.2–2.8)	3.6 (1.9–10.7)	53.2 (53.1–53.3)	30.3 (30.2–30.4)
226	0.95	1.2 (0.4–1.8)	1.1 (0.7–1.6)	53.3 (53.2–53.4)	30.2 (30.1–30.3)
228	0.99	1.3 (0.8–1.8)	1.1 (0.8–1.5)	53.5 (53.4–53.5)	30.4 (30.3–30.5)
229	0.97	0.7 (0.4–1.3)	4.1 (...–15.5)	53.1 (53.0–53.2)	30.3 (30.2–30.4)
231	0.85	0.8 (...–...)	0.9 (...–...)	53.4 (53.3–53.5)	30.4 (30.3–30.4)
237	0.91	1.8 (0.7–2.6)	1.2 (0.7–1.7)	53.4 (53.3–53.5)	30.3 (30.2–30.4)
255	0.85	1.0 (0.5–1.9)	2.2 (1.1–4.6)	53.0 (52.9–53.1)	30.0 (29.9–30.1)
256	0.79	2.2 (1.5–3.5)	10.0	53.1 (53.0–53.2)	30.2 (30.1–30.3)
259	0.92	0.8 (0.2–...)	0.9 (...–...)	53.5 (53.4–53.6)	30.5 (30.4–30.5)
261	0.72	2.2 (1.6–3.6)	1.7 (0.9–3.2)	53.9 (53.8–54.0)	30.9 (30.8–31.0)
264	0.98	1.2 (0.5–2.6)	4.0 (...–60.8)	53.0 (52.9–53.1)	30.1 (30.0–30.2)
265	0.43	0.7 (0.5–1.0)	0.7 (...–...)	53.5 (53.4–53.5)	30.4 (30.4–30.5)
268	0.71	1.2 (0.5–1.6)	0.4 (...–2.4)	53.7 (53.6–53.8)	30.6 (30.5–30.7)
270	0.46	0.9 (0.1–1.4)	1.0 (0.5–11.0)	53.0 (52.9–53.1)	30.0 (29.8–30.1)
277	0.99	2.9 (...–...)	1.7 (...–...)	53.7 (53.7–53.8)	30.7 (30.6–30.8)
281	0.93	0.1 (0.1–0.4)	4.8 (1.4–...)	52.4 (52.3–52.5)	29.6 (29.5–29.7)
286	0.97	1.2 (0.8–2.1)	2.9 (1.4–7.3)	53.2 (53.1–53.3)	30.2 (30.1–30.3)
289	0.94	1.2 (...–1.4)	1.1 (...–...)	54.2 (54.2–54.2)	31.1 (31.1–31.2)
293	0.95	0.4 (0.2–0.9)	4.2 (2.0–12.3)	52.8 (52.7–52.9)	30.0 (29.9–30.1)
295	0.84	2.2 (1.5–3.3)	10.0	53.1 (52.9–53.2)	30.2 (30.0–30.3)
296	1.00	0.3 (0.1–0.4)	2.3 (1.6–3.3)	53.2 (53.2–53.3)	30.2 (30.2–30.3)
301	0.97	0.5 (0.1–...)	0.7 (0.5–1.1)	53.5 (53.5–53.6)	30.5 (30.4–30.5)
304	0.99	0.6 (0.4–...)	2.9 (2.3–3.4)	53.9 (53.9–53.9)	31.0 (30.9–31.0)

Table 2. (Continued)

ID	Variable probability*	N_{H}^{\dagger} (10^{22} cm^{-2})	kT^{\ddagger} (keV)	$\log(EM^{\S})^{\dagger}$ (cm^{-3})	$\log(L_{\text{X}}^{\parallel})^{\dagger}$ (erg s^{-1})
305	0.94	1.4 (1.0–1.9)	20.2 (...-...)	53.8 (53.8–53.8)	31.1 (31.0–31.1)
307	0.82	0.6 (0.1–1.1)	0.9 (0.6–1.7)	53.0 (52.9–53.1)	30.0 (29.9–30.1)
309	0.99	0.3 (0.1–0.7)	3.4 (1.7–8.3)	52.8 (52.7–52.8)	29.9 (29.8–29.9)
310	0.99	0.5 (...-...)	1.6 (1.3–1.8)	54.2 (54.1–54.2)	31.1 (31.1–31.1)
311	0.99	0.6 (...-...)	1.5 (1.3–1.8)	54.0 (54.0–54.1)	31.0 (31.0–31.0)
313	0.94	0.2 (0.1–0.4)	1.6 (1.0–2.9)	53.2 (53.1–53.3)	30.2 (30.1–30.3)
317	0.99	0.6 (0.4–...)	1.9 (1.1–2.4)	53.4 (53.4–53.5)	30.4 (30.3–30.4)
320	0.99	0.2 (0.2–0.4)	2.1 (1.6–...)	53.5 (53.5–53.6)	30.5 (30.5–30.6)
321	0.92	1.4 (0.9–2.1)	4.9 (...–11.5)	53.4 (53.4–53.5)	30.6 (30.5–30.7)
329	0.78	0.4 (0.2–0.7)	1.3 (1.0–1.7)	53.1 (53.0–53.1)	30.0 (29.9–30.1)
331	0.82	3.6 (2.6–5.5)	23.1 (...-...)	53.7 (53.6–53.7)	31.0 (30.9–31.0)
333	0.99	0.3 (0.1–0.8)	1.5 (0.8–2.5)	53.2 (53.1–53.3)	30.2 (30.1–30.2)
344	0.96	0.2 (0.1–0.9)	1.2 (0.5–1.6)	52.8 (52.7–52.9)	29.8 (29.7–29.8)
347	1.00	0.2 (0.1–0.3)	29.8 (29.7–29.8)
349	0.99	1.7 (1.1–2.8)	0.9 (0.5–1.9)	53.4 (53.3–53.5)	30.4 (30.2–30.5)
350	1.00	1.3 (1.2–...)	4.3 (3.6–5.2)	54.5 (54.5–54.6)	31.7 (31.7–31.7)
351	0.99	0.6 (0.2–1.1)	0.9 (0.7–1.4)	53.1 (53.0–53.2)	30.0 (29.9–30.1)
353	0.60	1.0 (0.7–1.5)	10.0	53.2 (53.1–53.3)	30.3 (30.2–30.4)
354	0.99	1.0 (0.2–1.6)	1.0 (0.7–1.7)	53.2 (53.1–53.3)	30.1 (30.0–30.2)
355	0.56	0.8 (0.5–1.1)	0.5 (...-...)	53.3 (53.1–53.4)	30.2 (30.1–30.3)
357	0.88	4.2 (2.6–6.6)	10.0	53.2 (53.0–53.4)	30.3 (30.1–30.5)
358	0.99	0.8 (...-...)	1.0 (0.8–2.3)	53.7 (53.7–53.8)	30.7 (30.6–30.7)
359	0.96	1.0 (0.5–2.0)	28.3 (...-...)	52.9 (52.8–53.0)	30.2 (30.0–30.2)
360	1.00	0.5 (0.3–0.9)	3.7 (...–22.7)	52.8 (52.7–52.9)	30.0 (29.9–30.1)
363	0.99	2.2 (1.9–2.5)	2.8 (...–3.5)	54.4 (54.3–54.4)	31.4 (31.4–31.4)
366	0.63	0.8 (0.7–...)	1.7 (1.3–2.0)	54.1 (54.1–54.1)	31.0 (31.0–31.1)
367	0.91	0.6 (0.3–1.4)	2.1 (1.0–3.1)	53.2 (53.1–53.3)	30.2 (30.1–30.3)

* Variable probabilities obtained by a Kolmogorov–Smirnov test to the photons in the 0.5–10.0 keV band.

† 90% confidence limits are in parentheses. No value in a parenthesis means that the error is not constrained.

‡ If sources have no converged value of kT , we assume that they have $kT=10.0$ keV. For #347, the thin-thermal plasma model is rejected, while power-law model is accepted.

§ Emission measures.

|| Luminosity in the 0.5–10.0 keV band.

Table 3. X-ray properties along the evolutionary phases.

	CTTSs	WTTSs
Mon R2		
Number*	23 (12)	69 (45)
Variability [†] (ratio %)	8 (34.8)	23 (33.3)
N_{H} (10^{22} cm $^{-2}$) [‡]	1.3 (1.0)	0.9 (0.8)
kT_1 (keV) [‡]	3.1 (2.5)	1.9 (1.4)
kT_2 (keV) [‡]	2.4 (1.1)	2.0 (1.5)
ONC		
Number*	65 (56)	285 (250)
kT_1 (keV) [‡]	2.9 (1.5)	2.3 (1.4)
kT_2 (keV) [‡]	3.1 (1.6)	2.4 (1.4)
OMC-2/3		
Number*	14 (7)	92 (70)
kT_1 (keV) [‡]	2.1 (1.1)	1.4 (0.7)
kT_2 (keV) [‡]	1.5 (0.7)	1.3 (0.7)

* The number of sources that have N_{H} value of less than 10^{22} cm $^{-2}$ are given in parentheses. In the case of Mon R2, the number of the bright sources in each evolutionary phase are shown.

[†] The number of the time-variable sources. The fraction of the number of time-variable sources are given in parentheses.

[‡] The average of the best fit values (not weighted by the errors). The standard deviations are given in parentheses.

Table 4. X-ray properties of different stellar masses.

	High- and intermediate- mass	Low mass
Mon R2		
Number*	8	92
Variability [†] (ratio %)	3 (37.5)	33 (35.9)
N_{H} (10^{22} cm ⁻²) [‡]	2.6 (2.6)	1.0 (0.8)
kT (keV) [‡]	2.7 (1.9)	2.0 (1.4)
ONC		
Number	14	372
kT (keV) [‡]	3.1 (1.4)	2.4 (1.4)
OMC-2/3		
Number	9	94
kT (keV) [‡]	2.1 (1.2)	1.4 (1.2)

* The number of the bright sources in each mass range.

[†] The number of the time-variable sources. The fraction of the number of time-variable sources are given in parentheses.

[‡] The average of the best-fit values (not weighted by the errors). The standard deviations are given in parentheses.